Journal of Optoelectronics and Advanced Materials Vol. 6, No. 4, December 2004, p. 1287 - 1296

THE ANALYSIS OF THE INTERACTION METAL-SUPPORT IN Ni CATALYSTS BY EXTENDED X-RAY ABSORPTION FINE STRUCTURE AND X-RAY DIFFRACTION USING SYNCHROTRON RADIATION

N. Aldea*, B. Barz, A. C. Gluhoi, P. Marginean, X. Yaning[a], H. Tiandou[a], L. Tao[a], Z. Wu[a], Z. Wu[a]

National Institute for Research and Development of Isotopic and Molecular Technologies, 71-103 Donath, P.O. Box 700, 400293 Cluj-Napoca 5, Romania
[a]Beijing Synchrotron Radiation Facilities of Beijing Electron Positron Colider National Laboratory, Beijing, People's Republic of China

The supported Ni catalysts were analyzed by extended X-ray absorption fine structure and X-ray diffraction, in order to determine their local and global structure. The present study has pointed out a strong deformation of the local structure of the metal, due to its interaction with oxide support. The average particle size, the mean squares of the microstrain, the probability of the faults, the particle size distribution and microstrain functions of the supported Ni catalysts were determined by X-ray diffraction method. The method is based on Fourier analysis of the experimental X-ray line profiles (111), (200) and (220). The global structure is obtained with a fitting method based on generalized Fermi function facilities for approximation. The local and global microstructures of the catalysts are modified by the strong interaction between the metal clusters and oxide supports. As a result the chemisorption and catalytic processes which occur at the Ni-support interface are also changed.

(Received July 14, 2004; accepted November 29, 2004)

Keywords: Supported metal catalysts, X-ray diffraction, X-ray absorption near edge structure, Extended X-ray absorption fine structure, Catalytic activity

1. Introduction

The theoretical background of extended X-ray absorption fine structure (EXAFS) and X-ray diffraction (XRD) analysis are presented in the first section of the paper, including the main mathematical properties of the generalized Fermi function (GFF), used for approximation and deconvolution of the experimental X-ray line profiles (XRLP) [1-3]. The transmission EXAFS and XRD measurements were carried out at Beijing Synchrotron Radiation Facilities (BSRF) in 4W1B and 4W1C beam lines operating at 30-50 mA and and 2.2 GeV with an energy resolution of 1-3 eV at 10 KeV, at room temperature [4]. The x-ray wavelength for the XRD experiments was adjusted at 1.8276 Å. A NaI (Tl) detector was used and the signals were amplified and fed to a single channel analyzer (ORTEC 850) read out by a computer.

The present paper offers the complete local and global structure characterization by analyzing the first to forth coordination shells and (111), (200) and (220) XRLP using X-ray absorption spectroscopy and XRD methods. We have investigated the following systems: 60 at. % Ni/ZnO, 89.6 at. % Ni/UO_2, 88.4 at. % Ni/ThO_2, 60 at. % Ni/MgO, 80 at. % Ni/SiO_2, 70 at. % Ni/ZrO_2 and 85 at. % Ni/Al_2O_3.

* Corresponding author: naldea@L30.itim-cj.ro

The following preparation methods were used:

- coprecipitation at room temperature by addition of a water solution containing a mixture of nitrates of nickel and metal from support with a sodium hydroxide solution, under vigorous stirring, was applied to obtain the nickel on the support oxide. The nickel black was prepared by precipitation of a water solution of nickel nitrate with a sodium hydroxide solution;
- impregnation of the basic nickel carbonate with a water solution of uranyl nitrate [1,5].

2. EXAFS analysis

The electron wave vector *k* is related to the kinetic energy E and to the wavelength λ by:

$$k = (2mE)^{1/2} / \hbar = 2\pi / \lambda$$

The EXAFS function $\chi(k)$ is defined in terms of the atomic absorption coefficient by:

$$\chi(\mathrm{x}) = \frac{\mu(\mathrm{k}) - \mu_0(\mathrm{k})}{\mu_0(\mathrm{k})}$$

The theoretical EXAFS signal is defined by the relation:

$$\chi(\mathrm{k}) = \sum_{\mathrm{j}} \mathrm{A_j}(\mathrm{k}) \sin[2\mathrm{kr_j} + \delta_{\mathrm{j}}(\mathrm{k})]$$

where $$\mathrm{A_j}(\mathrm{k}) = \left(\frac{\mathrm{N_j}}{\mathrm{kr_j^2}}\right) \mathrm{F}(\mathrm{k},\mathrm{r},\pi) \exp[-2\mathrm{r_j} / \lambda(\mathrm{k})] \exp(-2\mathrm{k}^2\sigma_{\mathrm{j}}^2)$$

r_j - the radial distance, N_j - number of atoms in the j^{th} shell, $\delta_j(k)$ - the phase shift function, σ_j - the root mean square deviation of the distance about r_j, $F(k, r, \pi)$ - the back scattering and $\lambda_j(k)$ - the mean free path function for inelastic scattering.

The single shell contribution may be isolated by Fourier transform:

$$\Phi(\mathrm{r}) = (1/2\pi)^{1/2} \int_{\mathrm{k}_{min}}^{\mathrm{k}_{max}} \mathrm{k}^{\mathrm{n}} \chi(\mathrm{k}) \exp(-2\mathrm{ikr}) \mathrm{WF}(\mathrm{k}) \mathrm{dk}$$

where *WF(k)* - the window function used for the minimization of spurious errors.

The inverse Fourier transform of the radial structure function is obtained for any coordination shell by:

$$\chi_{\mathrm{j}}(\mathrm{k}) = (2/\pi)^{1/2} (1/\mathrm{k}^{\mathrm{n}}) \mathrm{WF}(\mathrm{k}) \int_{\mathrm{R_{1j}}}^{\mathrm{R_{2j}}} \Phi_{\mathrm{n}}(\mathrm{r}) \exp(2\mathrm{ikr}) \mathrm{dr}$$

The structural parameters for each coordination shell are determined by fitting the experimental spectrum with the theoretical function [1-5].

3. X-ray diffraction analysis

The method is based on the Fourier analysis of X - ray diffraction profiles (111), (200) and (220) using the Charlson approximation [1,3],

$$F(L)=1-L/D_{eff}-C^2\left\langle \varepsilon^2(L)\right\rangle_{hkl}L^2+C^2\left\langle \varepsilon^2(L)\right\rangle_{hkl}L^3/D_{eff}\ ,\ (L\to 0)$$

where $C^2=2\pi^2(h^2+k^2+l^2)/a^2$, D_{eff} - effective crystallite size, $\langle\varepsilon^2\rangle_{hkl}$ – mean square of the microstrain and F(L) are the module of the Fourier coefficients of the true sample obtained by deconvolution techniques from the experimental spectra and the instrumental function.

The particle size distribution function P(L) is obtained from the second derivative of the size Fourier transform:

$$D_{arith}=\int_{L\,min}^{L\,max} LP(L)dL$$

$$D_{harm}=\left[\int_{L\,min}^{L\,max}\frac{P(L)}{L}dL\right]^{-1}$$

where D_{arith} is the volumetric mean particle size and D_{harm} is the harmonic average particle size of the thickness of the particle normal to *(hkl)* reflecting planes.

The global structure is obtained with a new fitting method based on the GFF facilities for approximation and the Fourier transform of the experimental X-ray line profile and the instrumental function:

$$h(s)=\frac{A}{e^{-a(s-c)}+e^{b(s-c)}}\ ,$$

where *A*, *a*, *b*, *c* are unknown parameters and $s = 2\sin\theta/\lambda$ [1-3].

The integral width of the GFF distribution

$$\delta(a,b)=\frac{\pi}{\left(a^a b^b\right)^{1/(a+b)}\cos\left(\frac{\pi}{2}\frac{a-b}{a+b}\right)}$$

The module of the Fourier Transform

$$\left|F(\upsilon)\right|=\frac{A_h\rho_g}{A_g\rho_h}\sqrt{\frac{\cos^2\alpha+\sinh^2\beta\upsilon}{\cos^2\gamma+\sinh^2\delta\upsilon}}\ ,$$

where $\rho=\frac{a+b}{2}$, $q=\frac{a-b}{2}$, $\alpha=\frac{\pi q_g}{2\rho_g}$, $\beta=\frac{\pi^2}{\rho_g}$, $\gamma=\frac{\pi q_h}{2\rho_h}$ and $\delta=\frac{\pi^2}{\rho_h}$;

The true sample profile and its integral width

$$f(s^*)=\frac{2A_h\rho_g}{\pi A_g}\frac{\cos\frac{\pi\rho_h}{2\rho_g}\cosh\ \rho_h s^*}{\cos\frac{\pi\rho_h}{2\rho_g}+\cosh\ \rho_h s^*},$$

$$\delta(\rho_h, \rho_g) = \frac{\pi}{2\rho_h \cos\frac{\pi\rho_h}{2\rho_g}}\left(\cos\frac{\pi\rho_h}{\rho_g} + 1\right)$$

where the indexes *h, g* refer to the experimental and instrumental profiles.

4. Results and discussion

4.1 EXAFS results

Fig. 1 shows the absorption coefficients for investigated catalysts. The extraction of the EXAFS signal is based on E_0 determination followed by background removal before the pre-edge and after edge baseline fitting with different possible modeling functions. The local structure of these samples, corresponding to each coordination shell, has been determined by Fourier transform technique of the EXAFS function, defined in the range 20-150 nm^{-1}. The local structure of the standard Ni black powder for each coordination shell is described by the following parameters: N_1=12, R_1=0.249, N_2=6, R_2=0.352, N_3=24, R_3=0.431, N_4=12 atoms and R_4=0.497 nm, respectively.

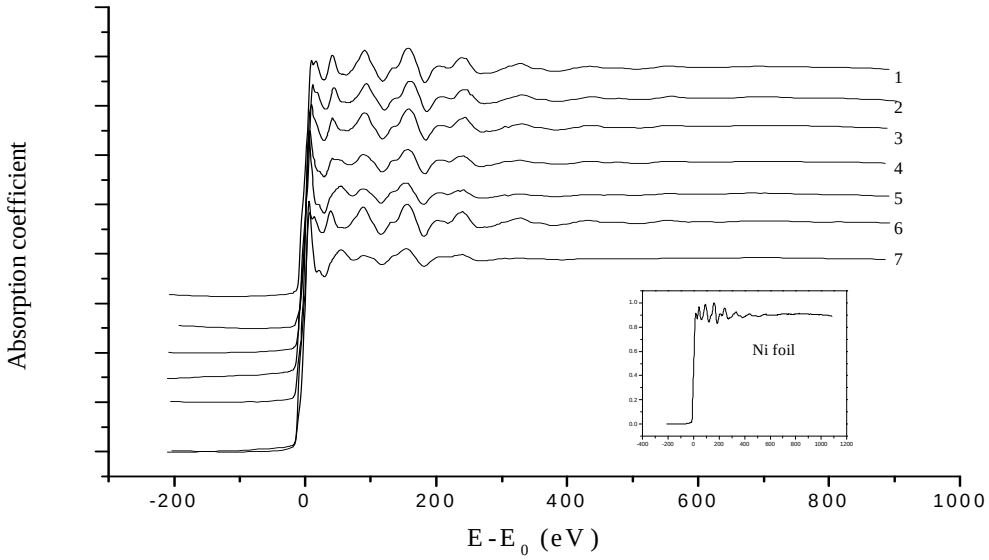


Fig. 1. The normalized absorption coefficients versus photoelectron energies: binding energy E_0 = 8332 eV, lower box - Ni foil as standard sample, (1)- 60 at % Ni/ZnO, (2) - 89.6 at % Ni/UO_2, (3) - 88.4 at % Ni/ThO_2, (4) - 60 at % Ni/MgO, (5) - 80 at % Ni/SiO_2, (6) - 70 at % Ni/ZrO_2, (7) - 85 at % Ni/Al_2O_3.

The diminution of the Fourier transform magnitude is a result of the reduced average coordination number. Each peak from |Ψ(r)| is shifted from the true distance due to the phase shift function which is included in the EXAFS signal. By assuming that each radial distribution function |Ψ(r)| can be a Gaussian distribution and based on Lavenberg-Marquard [1,5] fit, the total radial distribution function |Ψ(r)| is split into four contributions. Thus, the broadening and center of each coordination shell is represented in Fig. 2. By taking the inverse Fourier transform of the Gaussian distribution, given in Fig. 2, we obtained the experimental EXAFS function attached to each coordination shell. Then, the theoretical amplitude envelope and phase shift functions were extracted from a black nickel powder as a standard sample. Table 1 contains the best values of the local structural parameters for all the investigated coordination shells. In according with our previous

data, reported in [1,5], it was found that the average interatomic distances of the first to the forth coordination shells are closely related with the standard sample. The missing values are caused by the low signal/noise ratio. The atom number of the first shell decreases with 15% (88.4 at. % Ni/ThO_2) up to 49% (85 at. % Ni/Al_2O_3) relative to the standard sample. By analyzing the atom number of the second coordination shell, we also obtained a diminution between 8 % (60 at. % Ni/ZnO) and 38 % (60 at. % Ni/MgO). The structural model of the third coordination shell gives an increase of the atom number with 4 % for 60 at. % Ni/ZnO and a decrease between 22 % (70 at. % Ni/ZrO_2) and 46 % (60 at. % Ni/MgO). The last coordination shell shows a decrease between 14 % (88.4 at. % Ni/ThO_2) and 41 % (60 at. % Ni/MgO). Therefore, we consider that this diminution of the atom number is due to a strong interaction between the Ni atoms and the support surface. The metal-support interface influences the morphology and perhaps the electronic properties of the metal clusters. As a consequence the adsorption of the reactant molecules and the catalytic activity are modified [6,7].

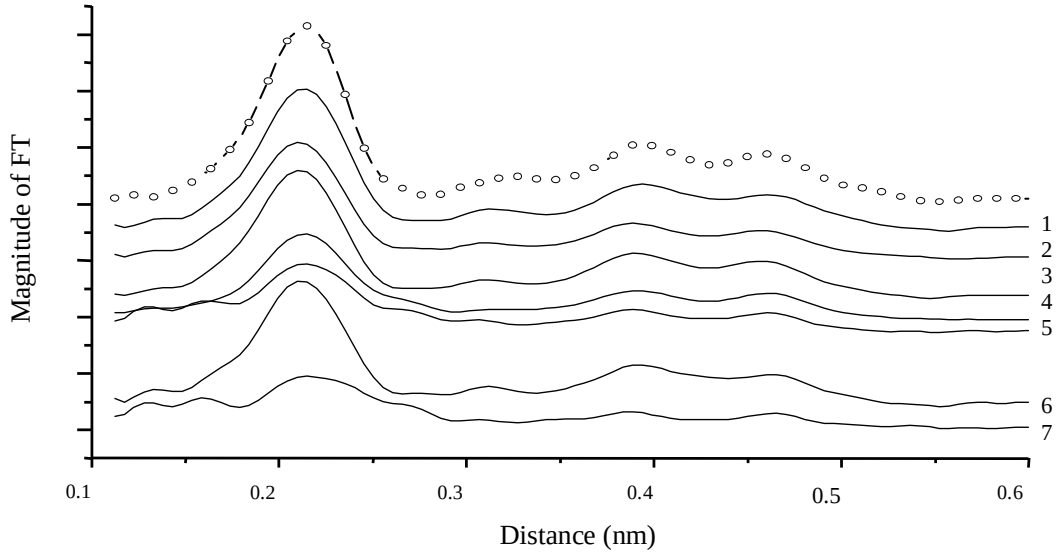


Fig. 2. The Fourier Transforms of the EXAFS spectra: (o) - Ni foil, (1)- 60 at % Ni/ZnO, (2) - 89.6 at % Ni/UO_2, (3) - 88.4 at % Ni/ThO_2, (4) - 60 at % Ni/MgO, (5) - 80 at % Ni/SiO_2, (6) - 70 at % Ni/ZrO_2, (7) - 85 at % Ni/Al_2O_3.

4.2 XRD results

The XRLP (111), (200) and (220) were processed in the manner of Ref. [1,3,5]. Their relative intensities with respect to the diffraction angle for standard sample as well as for the investigated samples are shown in Fig. 3. We have used for the first time the GFF for the XRLP approximation and its Fourier transform. In the former section we have shown that the coordination shell radii of the investigated samples have similar values as Ni standard sample. An additional proof of these results is the unchanged position and shape of each nickel K edge around 8333 eV; it means that all the samples contain only metallic nickel. These important results are strongly correlated with the positions of (111), (200) and (220) XRLP from experimental spectra presented in Fig. 3. Therefore, these results explain the metallic features of the investigated clusters, despite the strong deformation of the crystalline structure. Fig. 4 and 5 show the particle size distribution and microstrain functions for 60 at. % Ni/ZnO sample. The main results regarding the investigated supported nickel catalyst microstructure are summarised in Table 2. As a measure of the discrepancy between the XRLP, approximated by the GFF, pseudo-Voigt or Pearson VII, we defined a residual index [1,5]. By analysing the values of the residual index for each distribution, we have obtained similar results that demonstrate the validity and the reliability of the GFF approximation.

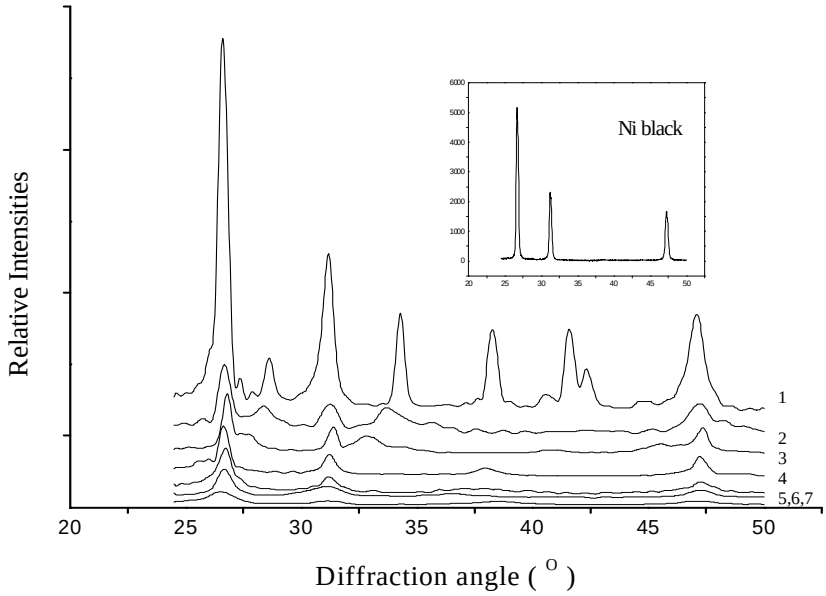


Fig. 3. The relative intensities of (111), (200) and (220) experimental XRD line profiles: upper box - Ni black as instrumental function, 1- 60 at % Ni/ZnO, 2 - 89.6 at % Ni/UO_2, 3 - 88.4 at % Ni/ThO_2, 4 - 60 at % Ni/MgO, 5 - 80 at % Ni/SiO_2, 6 - 70 at % Ni/ZrO_2, 7 - 85 at % Ni/Al_2O_3.

The integral width of the XRLP increases as the particle size decreases. Additionally, the crystallite size increases while the mean square of the microstrain and the stacking fault probability decrease. The values of the crystallite size can be correlated with the mean value of the grain diameter [8,9], if we take into consideration the physical meaning of the crystallite size and the grain size. It is possible that a grain of nickel cluster is built up of more nickel crystallites. In this case, the probability of hydrogen adsorption on the crystallites interface, inside the metal cluster, is much reduced. After the calibration of the experimental XRLP we have observed a shift in the peak position compared to the standard sample. The XRLP from these samples can be more accurately indexed as a tetragonal lattice than the one of Ni standard; this denotes a deformation of the cubic structure. We selected the weighted least square method to calculate the lattice parameters in order to minimise the calculation errors. The equation is derived from the Bragg's law and given by

$$\frac{h^2+k^2}{a^2}+\frac{l^2}{c^2}+D\cos^2(2\theta)=\frac{4\sin^2(\theta)}{\lambda^2},$$

where a, b, c are the lattice parameters, h, k, l the Miller indices, θ is the diffraction angle, D is a drift constant and λ is the wavelength of the incident radiation. The measure of the deformations is given by the absolute value of the relative variations (AVRV), ε, of the cell parameters. These values, for each sample, are contained in the bottom part of Table 2. By analysing the AVRV we have obtained the following relation:

$$\varepsilon_{Ni/Sio_2} < \varepsilon_{Ni/ZnO} < \varepsilon_{Ni/ThO_2} < \varepsilon_{Ni/MgO} < \varepsilon_{Ni/UO_2} < \varepsilon_{Ni/ZrO_2} < \varepsilon_{Ni/Al_2O_3},$$

while the average effective crystallite sizes have the following succession:

$$D_{Ni/Al_2O_3} < D_{Ni/ZrO_2} < D_{Ni/SiO_2} < D_{Ni/UO_2} < D_{Ni/ZnO} < D_{Ni/MgO} < D_{Ni/ThO_2}.$$

We can observe that the transition from the cubic system to the tetragonal one increases with the average crystallite size for the catalysts Ni/SiO_2, Ni/ZnO, Ni/ThO_2, while for the Ni/MgO, Ni/UO_2, Ni/ZrO_2, Ni/Al_2O_3 the effective crystallite size decreases. We have tried to build a model to explain the correlation between the AVRV and the crystallite size of the investigated systems, but we have not found a reliable one yet.

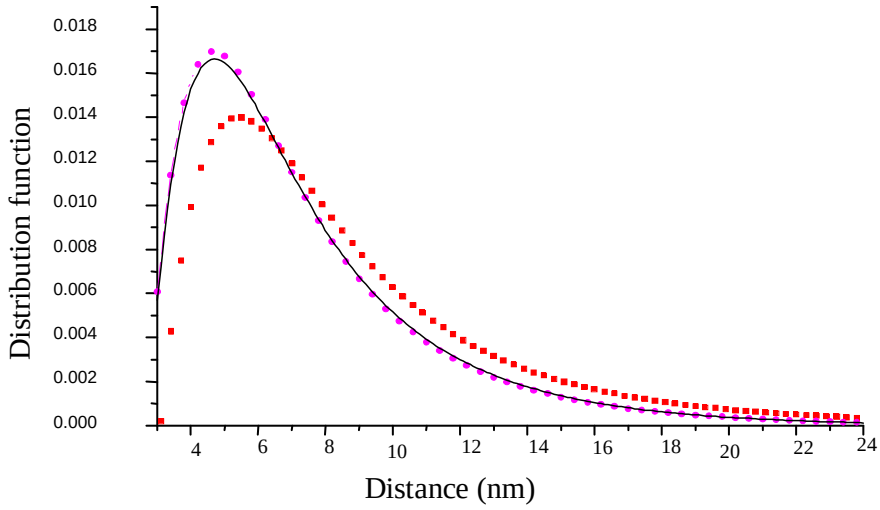


Fig. 4. The crystallites distribution function for Ni/ZnO: ■ (111), ● (200) and — (220) X-ray line profiles.

Beside the (111), (200) and (220) profiles of the supported Ni we have found additional lines due to the support, such as ZnO that is best crystallised, followed by Al_2O_3, the others being less crystallised.

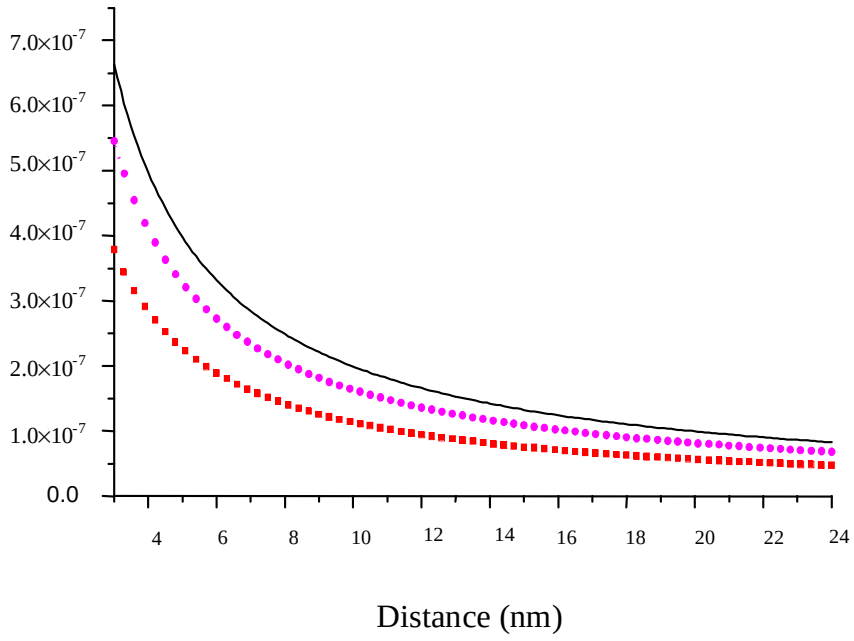


Fig. 5. The microstrain distribution function for Ni/ZnO: ■ (111), ● (200) and — (220) X-ray line profiles.

The crystallisation degree of the supports resulted from XRD measurements can be correlated with the particle size obtained from the surface area data determined by krypton and hydrogen adsorption [9].

5. Conclusions

The data presented in this paper describe the whole local and global structure of supported nickel catalysts determined by EXAFS and XRD analysis. The results give a complete image of the strong deformation of the crystalline structure. The conclusions that can be drawn from these studies are:

(i) The local structure of the investigated systems shows a strong morphological deformation of the nickel clusters caused by metal-support interaction. These morphological modifications could be accompanied by the modification of the electronic structure that has a large effect on the reactant absorption. As a result of these modifications induced by supports is an enhancement of the catalytic activity for H/D exchange reaction between hydrogen and water vapor.

(ii) By the investigation of the XRLP of the supported nickel catalysts we could obtain the crystallite size, the microstrain and the lattice distortion. The last one could be due to the strong interaction between the metal clusters and the oxide support. The global parameters of the microstructure, obtained from (111), (200) and (220) XRLP, show the reliability of the GFF distribution.

Table 1. The local structural parameters of the investigated samples.

Sample	Shell	R±ΔR Shell radius(nm)	N±ΔN Atomic numbers
60 at % Ni/ZnO	1	0.25±0.01	1 0±0.1
89.6at%Ni/UO_2		0.25± 0.01	9.01±0.1
88.4 at % Ni/ThO_2		0.25±0.01	10.15±0.12
60 at % Ni/MgO		0.25±0.005	7.17±0.1
80 at % Ni/SiO_2		0.25±0.006	9.32±0.11
70 at % Ni/ZrO_2		0.25±0.003	9.16±0.2
85 at % Ni/Al_2O_3		0.256±0.001	6.08±0.12
60 at % Ni/ZnO	2	0.35±0.01	5.53±0.1
89.6at%Ni/UO_2		0.351±0.03	4.32±0.05
88.4 at % Ni/ThO_2		0.349±0.02	4.46±0.02
60 at % Ni/MgO		0.352±0.01	3.73±0.04
80 at % Ni/SiO_2			
70 at % Ni/ZrO_2		0.35±0.02	4.46±0.02
85 at % Ni/Al_2O_3			
60 at % Ni/ZnO	3	0.433±0.008	25.05±0.03
89.6at%Ni/UO_2		0.433±0.05	17.58±0.022
88.4 at % Ni/ThO_2			
60 at % Ni/MgO		0.432±0.007	12.92±0.03
80 at % Ni/SiO_2			
70 at % Ni/ZrO_2		0.433±0.01	18.64±0.04
85 at % Ni/Al_2O_3			
60 at % Ni/ZnO	4	0.499±0.001	9.1±0.1
89.6at%Ni/UO_2		0.498±0.001	10.10±0.05
88.4 at % Ni/ThO_2		0.5±0.003	10.34±0.02
60 at % Ni/MgO		0.5±0.001	7.09±0.01
80 at % Ni/SiO_2			
70 at % Ni/ZrO_2		0.502±0.003	10.10±0.05
85 at % Ni/Al_2O_3			

Table 2. The global structural parameters of the investigated samples

Name of sample	$\delta_f(\rho_h,\rho_g)$ $(nm)^{-1}$	$D_{eff}^{(hkl)}$ (nm)	$\langle\varepsilon^2\rangle_{hkl}\times10^{-4}$	$D_{arith}^{(hkl)}$ (nm)	$D_{harm}^{(hkl)}$ (nm)	SFP (%)
(111) XRLP, δ_g=0.00299 nm^{-1}						
60 at % Ni/ZnO	0.075	9.5	0.14	9	7.3	0.2
89.6 at%Ni/UO_2	0.963	7.3	0.22	7.2	5.9	0.0
88.4 at % Ni/ThO_2	0.728	10.4	0.12	9.3	7.5	7
60 at % Ni/MgO	0.07	10.2	0.13	9.4	7.5	0.4
80 at % Ni/SiO_2	0.134	5.9	0.36	4.9	4.1	0.3
70 at % Ni/ZrO_2	0.141	5.1	0.41	5.1	4.2	1.4
85 at % Ni/Al_2O_3	0.228	3.2	1.04	3.1	2.6	1.3
						0.0
						4
(200), δ_g=0.0031 nm^{-1}						
60 at % Ni/ZnO	0.093	7.9	0.14	7.5	6.1	0.2
89.6 at%Ni/UO_2	0.104	6.9	1.8	6.8	5.6	0.1
88.4 at % Ni/ThO_2	0.083	8.8	0.12	8.2	6.7	0.3
60 at % Ni/MgO	0.104	6.7	0.19	6.7	5.5	0.1
80 at % Ni/SiO_2	0.164	4.7	0.37	4.4	3.7	0.6
70 at % Ni/ZrO_2	0.241	2.9	1.01	2.9	2.4	0.8
85 at % Ni/Al_2O_3	0.214	3.4	0.73	3.2	2.7	0.7
(220), δ_g=0.0028 nm^{-1}						
60 at % Ni/ZnO	0.112	6.8	0.1	6.6	5.4	0.2
89.6 at%Ni/UO_2	0.104	3.9	0.34	3.4	2.7	1.5
88.4 at % Ni/ThO_2	0.083	8.1	0.4	7.8	6.4	0.1
60 at % Ni/MgO	0.096	7.9	0.06	7.7	6.3	9
80 at % Ni/SiO_2	0.163	4.5	0.20	4.3	3.6	0.1
70 at % Ni/ZrO_2	0.179	4.2	0.24	4.2	3.5	3
85 at % Ni/Al_2O_3	0.228	3.2	0.4	3.2	2.7	0.4
						2
						0.8
						9
						1.5
Average particle size						
60 at % Ni/ZnO		8		8	6	
89.6 at%Ni/UO_2		6		6	5	
88.4 at % Ni/ThO_2		9		8	7	
60 at % Ni/MgO		8		8	6	
80 at % Ni/SiO_2		5		5	4	
70 at % Ni/ZrO_2		4		4	3	
85 at % Ni/Al_2O_3		3		3	3	
	a (nm)	c(nm)	$\varepsilon=\lvert(a\text{-}c)/a\rvert$ (%)	D x 10^{-2}		
60 at % Ni/ZnO	0.35491	0.35436	0.15	-0.39147		
89.6 at%Ni/UO_2	0.35243	0.34232	2.86	-1.53470		
88.4 at % Ni/ThO_2	0.35250	0.35128	0.34	-0.39155		
60 at % Ni/MgO	0.35314	0.35771	1.29	-0.24984		
80 at % Ni/SiO_2	0.35351	0.35302	0.13	-0.54444		
70 at % Ni/ZrO_2	0.35349	0.34040	3.7	-1.78453		
85 at % Ni/Al_2O_3	0.35436	0.40760	15.2	-3.66647		

$\delta_g(\rho_g)$ - integral width for standard black Ni powder, $\delta_f(\rho_h, \rho_g)$ - integral width for true samples, $D_{eff}^{(hkl)}$ - effective particle size, $\langle\varepsilon^2\rangle_{hkl}$ - mean square of the microstrain, $D_{arith}^{(hkl)}$ - arithmetic average particle size, $D_{harm}^{(hkl)}$ - harmonic average particle size, $SFP^{(hkl)}$ - stacking fault probability (Ref. 1 contains the meaning of each parameters).

References

[1] N. Aldea, A. Gluhoi, P. Marginean, C. Cosma, X. Yaning, Spectrochim Acta Part B **55**, 997 (2000).
[2] N. Aldea, C. Tiusan, R. Zapotinschi, Proceedings of the 8th Joint EPS-APS International Conference on Physics Computing, Published by Academic Computer Center CYFRONET-Krakow, September 1966, 391.
[3] N. Aldea, C. Tiusan, B. Barz, J. Optoelectron. Adv. Mater. **6**(1) 225 (2004).
[4] B. S. R. F. Activity Report 2001, Beijing Electron Positron Collider National Laboratory.
[5] N. Aldea, A. Gluhoi, P. Marginean, C. Cosma, X. Yaning, H. Tiandou, W. Wu, B. Dong, Spectrochim. Acta Part B **57**, 1453 (2002).
[6] B. Barz, A. Gluhoi, P. Marginean, N. Aldea, X. Yaning, B. Dong, CERES Program, Annual Scientific Session, Dec. 2-3, 2002, Bucharest.
[7] D. C. Koningsberger, B. C. Gates, Catal. Lett. **14**, 271 (1992).
[8] G. A. Somorjai, Surf. Sci. **335**, 10 (1995).
[9] P. Marginean, A. Olariu, J. Catal. **95**, 1 (1985).